RESEARCH

Oxidation of a Mo-Si-B-Ti Alloy

Longfei Liu[1] · Liam F. Wood[1] · Phalgun Nelaturu[1] · Tianrui Duan[1] · Chuan Zhang[2] · Fan Zhang[2] · Dan J. Thoma[1] · John H. Perepezko[1]
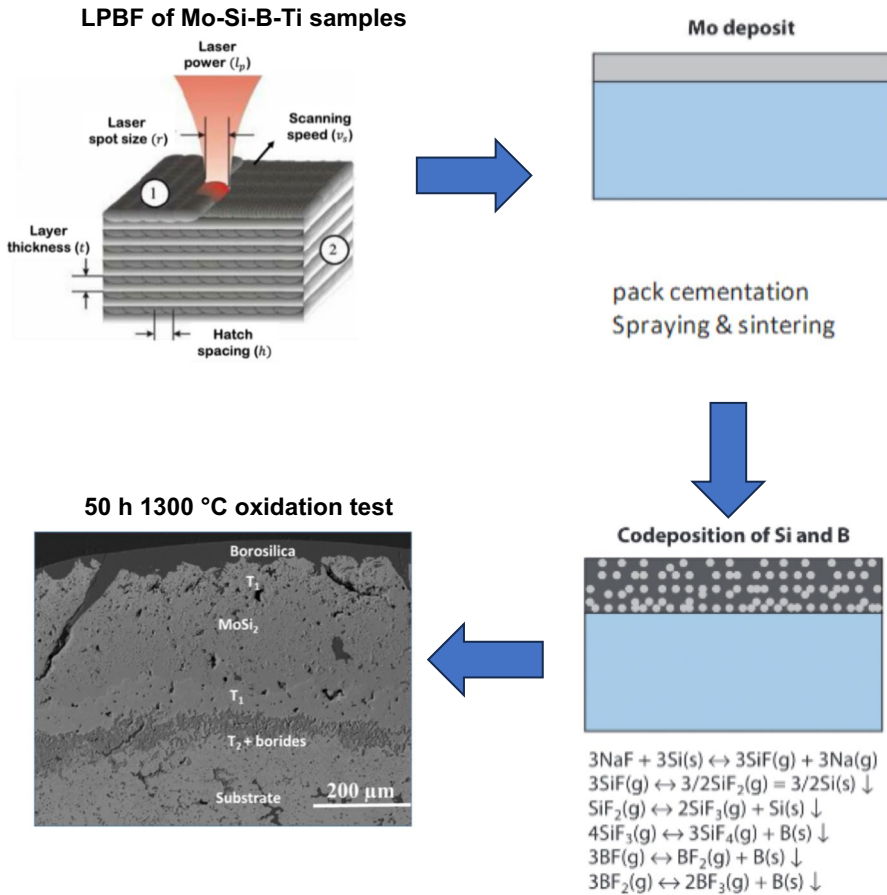
Abstract

The oxidation of a titanium (Ti)-modified Mo-Si-B alloy designed for aerospace applications was investigated. Test samples were produced using arc melting and laser powder bed fusion (LPBF) additive manufacturing methods. To address high-temperature oxidation, a three-step coating strategy was employed, comprising a Mo precoat, Si and B co-deposition, and a conditioning step for the formation of a self-healing coating. The study evaluates the oxidation resistance of both uncoated and coated Mo-Si-B-Ti alloys at temperatures ranging from 1100 to 1300 °C. Uncoated alloys exhibited catastrophic mass loss within 10 hours at temperatures between 800 and 1300 °C. In contrast, the coated samples demonstrated minimal mass loss at 1300 °C after 50 hours, with only minor mass gain observed under cyclic thermal loading after 300 cycles. Microstructural analysis revealed distinct differences between arc-melted and LPBF samples, with the latter displaying an ultrafine dendritic microstructure. The applied coating effectively prevented oxygen diffusion into the substrate, even at elevated temperatures, showcasing its protective capabilities. During cyclic tests, the coating exhibited a self-healing mechanism, with cracks filled with borosilica contributing to prolonged environmental resistance.

Extended author information available on the last page of the article

Published online: 22 August 2024

Springer

Graphical Abstract

LPBF of Mo-Si-B-Ti samples

50 h 1300 °C oxidation test

Mo deposit

pack cementation
Spraying & sintering

Codeposition of Si and B

$$3NaF + 3Si(s) \leftrightarrow 3SiF(g) + 3Na(g)$$
$$3SiF(g) \leftrightarrow 3/2SiF_2(g) = 3/2Si(s) \downarrow$$
$$SiF_2(g) \leftrightarrow 2SiF_3(g) + Si(s) \downarrow$$
$$4SiF_3(g) \leftrightarrow 3SiF_4(g) + B(s) \downarrow$$
$$3BF(g) \leftrightarrow BF_2(g) + B(s) \downarrow$$
$$3BF_2(g) \leftrightarrow 2BF_3(g) + B(s) \downarrow$$

Introduction

Mo-based alloys such as those in the Mo-Si-B system present an opportunity to replace Ni-based superalloys for future aerospace applications, where the increased melting temperature will allow for increased efficiency of the gas turbine engines. While alloy compositions composed of the Mo_{ss} (solid solution), Mo_3Si and Mo_5SiB_2 (T_2) phases exhibit high-temperature strength and some oxidation resistance due to the formation of a borosilica scale, they suffer from low ductility and fracture toughness at room temperature [1–8]. The mechanical properties can be improved significantly by shifting the alloy design to the
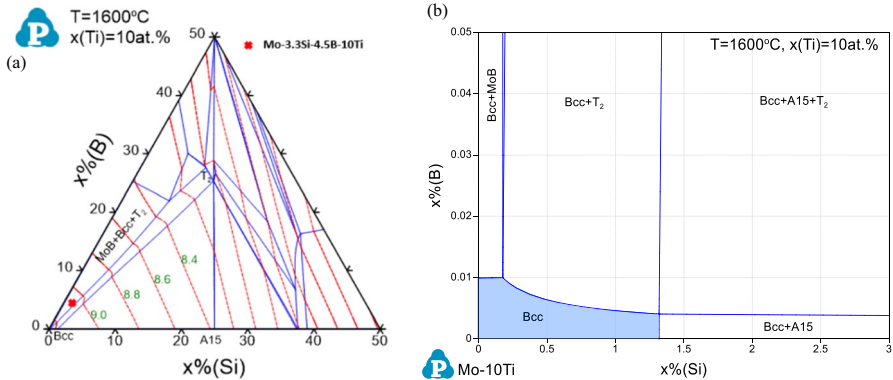
Fig. 1 Pandat phase diagram for Mo-Si-B at 10 at.% Ti: **a** phase regions in the Mo corner, density contours as provided in red, **b** enlarged Mo corner to show solubility in Mo

three-phase region with the Mo_{ss}, Mo_2B and T_2 phases where the Si solubility in the Mo_{ss} phase is reduced by about 50% [9, 10]. To reduce the alloy density, a substitution of Ti for Mo at the 10 at. % level in a Mo-3.3Si-4.5B-10Ti composition brings the density to about 9 gm/cm^2 as shown in Fig. 1a which is comparable to current Ni base superalloys. Moreover, the Ti substitution also results in a further reduction in the Si solubility in the Mo_{ss} based upon the Pandat calculation in Fig. 1b.

While laboratory test samples can be produced by arc melting, the scale up to component sizes is facilitated by employing additive manufacturing (AM) methods. Often the improvement in one performance metric such as ductility has an effect on other performance behavior; thus, it is important to evaluate the effect of the new alloy design on the oxidation performance. As the base alloy only has 3.3 at. % Si, implementing a coating strategy becomes essential to combat environmental attack. However, the coating must not only offer protection against environmental factors but also demonstrate compatibility with the thermodynamics and mechanics of the Mo-Si-B-Ti alloy. The Mo-Si-B coating has been validated as a robust and oxidation-resistant solution, effectively safeguarding both alloys and ceramics even at extremely high temperatures (up to 1700 °C) [11]. This protection extends to various environments, including air, water vapor and complex conditions such as CMAS (CaO-MgO-Al$_2$O$_3$-SiO$_2$, typical molten silicate deposits) [12, 13]. Through a two-step strategy, this coating has been successfully applied to numerous refractory alloys, ensuring prolonged environmental resistance under elevated temperatures [14]. In this study, to examine the effects of Ti addition, both the uncoated and coated Mo-Si-B-Ti alloys were exposed to oxidation from 800 to 1300℃ and analyzed to elucidate the oxidation mechanism.
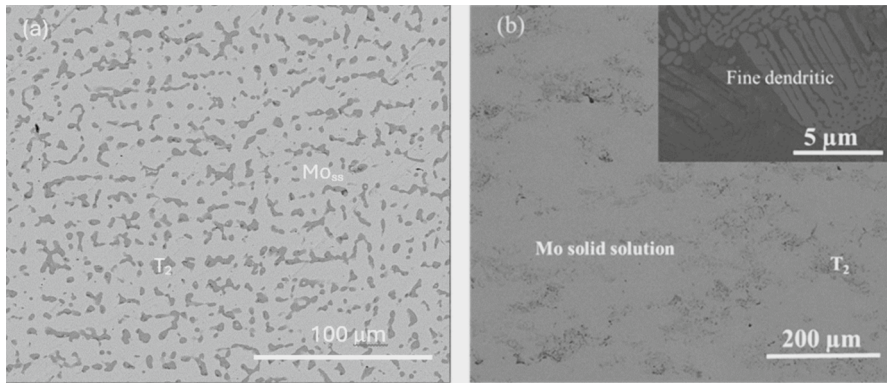
Fig. 2 Microstructure of arc-melted **a** and LPBF **b** Mo-3.3Si-4.5B-10Ti samples
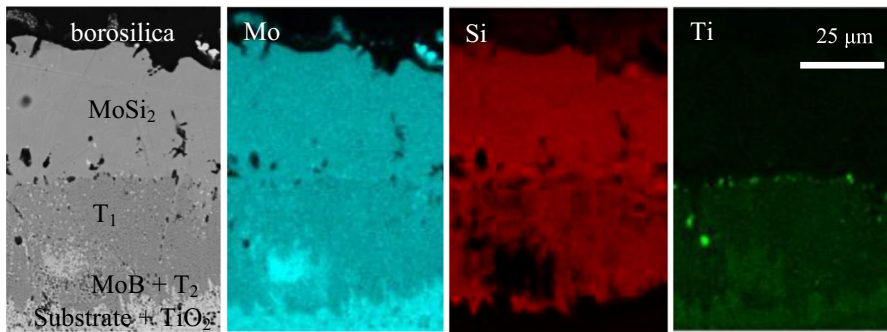

Fig. 3 Packed and conditioned structure on LBPF Mo-Si-B-Ti sample with Mo, Si, and Ti EDS maps

Experimental Procedures

Samples were made using both arc melting and additive manufacturing, using a laser powder bed fusion (LPBF) on an EOS 290 facility. The arc-melted samples were produced by arc melting elemental Mo, Si, B and T into a 20-g ingot. This ingot was melted five times to homogenize the sample. Pieces of the ingot were melted into a spherical shape with a diameter of approximately 3 mm. The AM samples were fabricated by a reactive synthesis involving the reaction of Mo, Si_3N_4, BN and Ti powders [15]. The AM processing was guided by the application of a dimensionless number that enables the selection of the optimum processing parameters as scan speed at 800–1200 mm/s, laser power at 200–320 W and hatch spacing at 0.07 mm and 0.09 mm [15]. Plates of the alloy were printed with dimensions of 8 cm × 6 cm × 0.2 cm. This plate was then cut into 48 samples with dimensions approximately 1.2 cm × 1 cm × 0.2 cm for testing.

To improve the oxidation resistance of the alloy, a three-step coating is applied onto the sample, where the sample is first coated with a Mo powder precoat using

a slurry application, followed by sintering under vacuum at 1450 ℃ for 30 min. This is followed by the co-deposition of Si and B sources using pack cementation with a NaF activator and Al_2O_3 powder filler, at 1000 ℃ for 50 h in flowing Ar, with a 15 ℃/min heating rate and furnace cooling [16]. The coating is finished with a conditioning step, where the coating is oxidized to form a multilayer, self-healing coating. The conditioning was conducted in ambient lab air, at 1300 ℃ for 10 h, with a 15 ℃/min heating rate and furnace cooling. The oxidation was studied both isothermally and under cyclic thermal loading. The isothermal oxidation testing was performed using a Mettler Toledo TGA/DSC 3 +. Temperature ramp rates to the isotherm were + 70 ℃/min for heating and − 70℃/min for cooling. Cyclic oxidation testing was performed in an open-air tube furnace at 1300 ℃. One cycle is 1 h inside of the furnace, and 3 min outside of the furnace, where the sample temperature drops below 150 ℃ as measured by a thermocouple.

The microstructures of all samples were observed by scanning electron microscopy (Zeiss Gemini-450 FESEM and Hitachi S-3400N Type-II) with backscattered electron images. Qualitative compositional data was obtained using an Oxford 35 mm^2 SDD energy-dispersive X-ray spectrometer (EDS). The chemical compositions of the constituent phases in the studied alloys were measured using a CAMECA SX50 electron microprobe operated at an accelerating voltage of 6 kV and a current of 6.3×10^{-9} A. The calibration standards consisted of 99.9% pure Mo, Si, B and Ti elements. The Mo Lα and Ti Kα peaks were analyzed with a PET crystal, Si Kα with a TAP crystal and B Kα with a PC2 crystal. The B concentration was quantified by separating the intensity of the B Kα peak (at 0.182 kV) from the Mo Mζ peak (at 0.192 kV) using the analysis software Probe for Windows (Advanced Microbeam Inc) and following the procedure described previously. Probe sizes ranging from 1.2 to 20 μm at 900 pA were used to measure the compositions of constituent phases and solidified zones (with a fine-scale solidification microstructure), respectively.
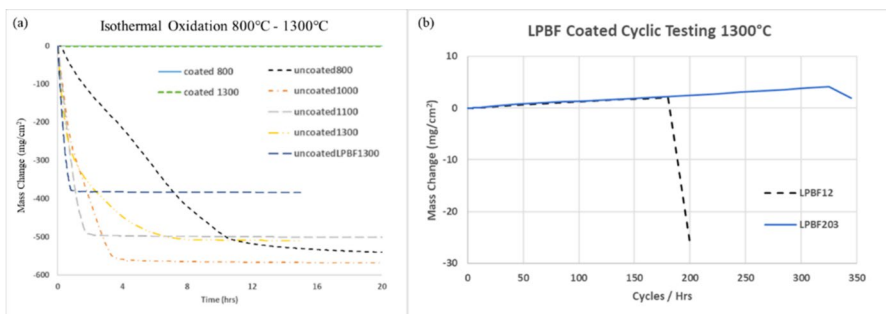

Fig. 4 **a** TGA curves of samples oxidized at 800–1300 °C **b** cyclic oxidation test of coated sample at 1300 °C
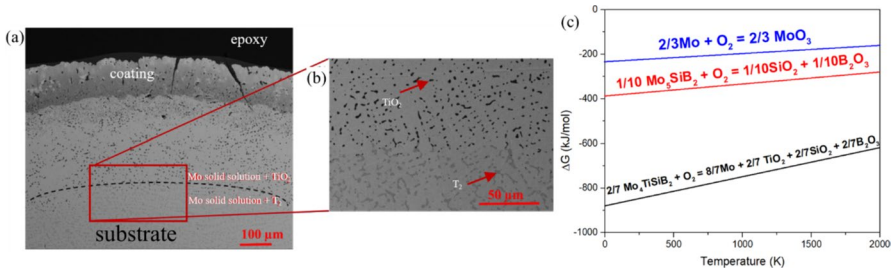
Fig. 5 **a** Coated arc-melted Mo-Si-B-Ti sample oxidized at 1300 °C for 50 h in TGA **b** enlarged interface of $Mo_{ss}+TiO_2$ and $Mo_{ss}+T_2$ **c** Gibbs free energy plot of phase reactions with oxygen explaining the interface in (b)

Results and Discussion

Microstructure

Figure 2 shows the microstructure of the arc-melted Mo-3.3Si-4.5B-10Ti sample and the LPBF Mo-3.3Si-4.5B-10Ti sample. Figure 2a shows the arc-melted sample, with the lighter color Mo solid solution phase and the darker color T_2 phase with Ti. The average grain size of arc-melted sample is about 40 µm. In Fig. 2b, the LPBF sample exhibits the same phases as the arc-melted sample. The LPBF sample has an ultrafine dendritic microstructure with a secondary dendritic spacing of about 400 nm, while the arc-melted sample had a larger dendrite spacing of about 4 µm.

The coated samples exhibit a multiphase microstructure as indicated in the cross section of Fig. 3. The coating structure involves a multiphase layer arrangement from the substrate alloy with the Mo_5SiB_2 (T_2) phase + MoB followed by the Mo_5Si_3 (T_1) phase and the $MoSi_2$ phase underneath the outer borosilica scale.
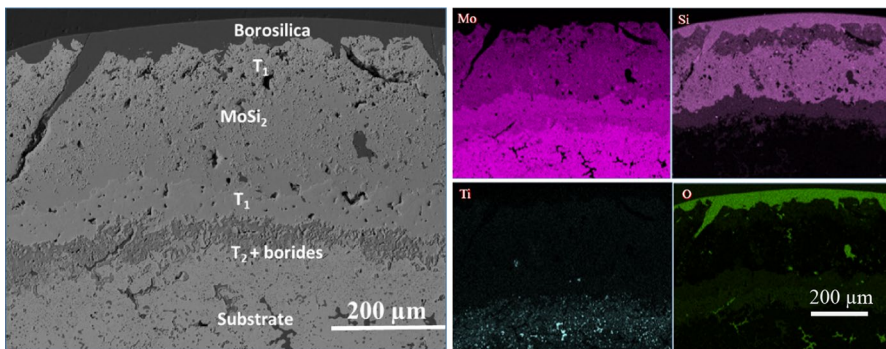

Fig. 6 EDS map of coated arc-melted Mo-3.3Si-4.5B-10Ti sample oxidized at 1300 °C for 50 h
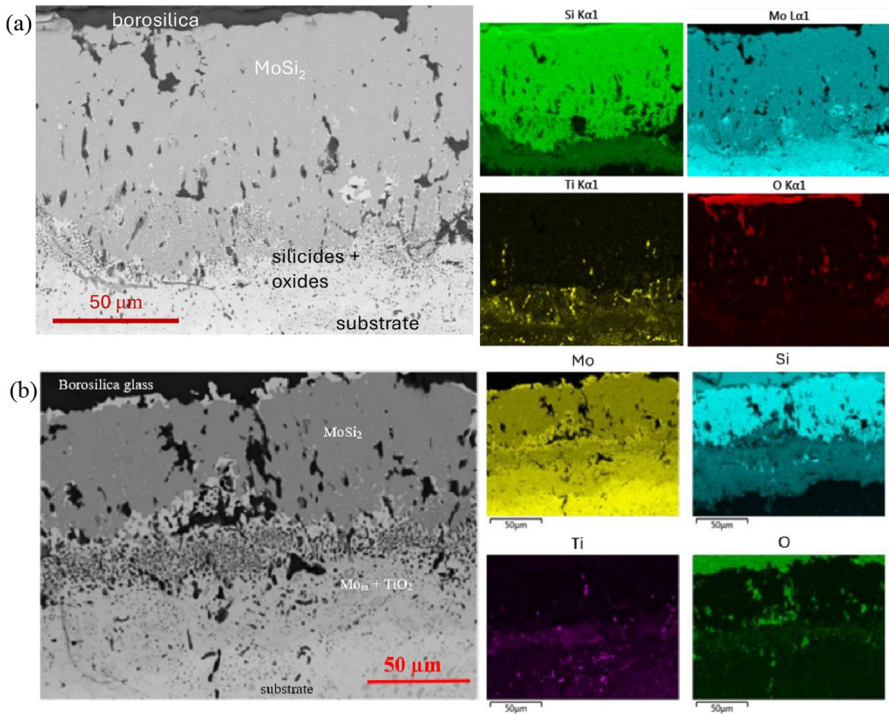
Fig. 7 Coated LPBF Mo-3.3Si-4.5B-10Ti sample oxidized at **a** 800 °C and **b** 1300 °C for 100 h

The small dark regions in the disilicide layer are voids leftover from the Mo pre-coat and the pack cementation coating process.

Oxidation

The oxidation of the uncoated alloy results in catastrophic mass loss for both arc-melted and LPBF samples. Figure 4a shows that for temperatures between 1000 °C
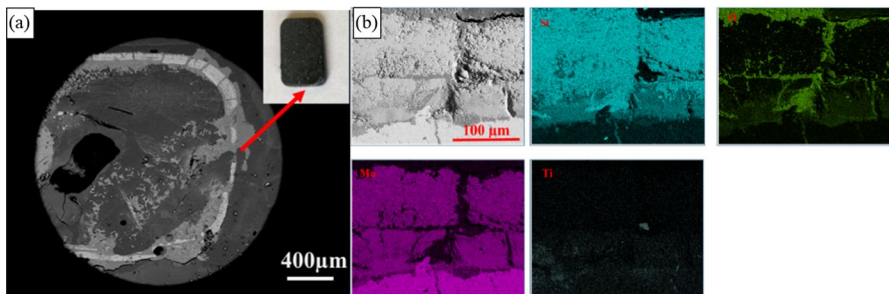

Fig. 8 **a** Large-scale image showing location of cyclic sample failure **b** EDS mapping coated LPBF Mo-3.3Si-4.5B-10Ti sample oxidized at 1300 °C for 180 cycles

and 1300 °C, total mass loss of uncoated samples is reached after only 5 h. At 800 °C, total mass loss is reached after 10 h. This is represented as a plateau in the TGA curve, where only SiO_2 and TiO_2 sponge remain. Following pack cementation, the addition of Ti in the substrate results in the formation of TiO_2 during the conditioning oxidation step. The presence of TiO_2 during the conditioning step does not allow the continuous protective borosilica to form and thus the coating is not protective. To address the effect due to the Ti addition, a Mo-slurry coating is required before the protective pack cementation coating can be applied to reduce the Ti concentration at the surface of the substrate and at the interface of the coating. With the application of the coating, the sample has minimal loss at both 800 °C and 1300 °C after 50 h. Under cyclic thermal loading (Fig. 4b), two samples show a very minor linear mass gain up to 345 cycles, where it has gained 4.15 mg/cm². The reason for this can be explained by continued growth of the outermost glassy layer as cracks in the coating continue to self-heal. Upon a crack reaching a critical size where the glass can no longer protect the substrate, a large mass loss is seen, as shown by the dashed black line in Fig. 4b. Testing for the sample that reached 345 cycles was stopped prematurely.

In the substrate, the presence of oxygen can react with Ti and forms some TiO_2 in the interdendritic region. The boundary of the Mo solid solution + TiO_2 and the Mo solid solution + T_2 in the coated arc-melted Mo-3.3Si-4.5B-10Ti sample oxidized at 1300 °C for 50 h is shown in Fig. 5. Based upon the Ellingham diagram (Fig. 5c), the oxygen partial pressure to form TiO_2 at this boundary is about 10^{-21} atm. This interface is about 500 μm below the outer borosilica surface. The existence of the boundary demonstrates that the coating is very effective for preventing O diffusion into the substrate even at elevated temperatures.

At 800 °C, the coated sample is barely oxidized and the borosilica layer thickness is only 5 μm. Most of the $MoSi_2$ layer remains the same and the transformation of $MoSi_2$ to T_1 and T_2 layers has just started. The volume change causes some voids inside the $MoSi_2$ and some MoO_2 forms in the voids.

Following oxidation at 1300°C for 50 h Fig. 6 shows EDS mapping coated arc-melted Mo-3.3Si-4.5B-10Ti sample. The outer borosilica layer thickness is about
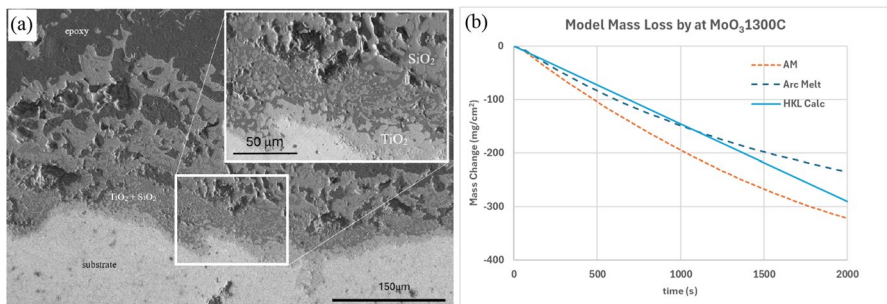

Fig. 9 **a** Uncoated arc-melted sample oxidized at 1300 °C for 1 h. **b** Linear mass loss region of uncoated isothermal oxidation of arc-melted and LPBF Mo-3.3Si-4.5B-10Ti sample modeled by examination of MoO_3 evaporation from the substrate

30 μm. A layer of T_1 (Mo_5Si_3) phase was formed between the borosilica layer and unreacted $MoSi_2$ layer. Another T_1 layer was formed underneath the $MoSi_2$ layer and a T_2+boride layer between the T_1 layer and the substrate.

The development of TiO_2 can be related to the oxidation of the T_2 phase which forms in the interdendritic regions as the final solidification product. Based upon the estimated free energy for the T_2 phase [17, 18] and tabulated values for TiO_2, SiO_2 and B_2O_3 [17, 18], the relevant oxidation reactions can then be assessed as displayed in Fig. 5c. The plot in Fig. 5c demonstrates that the oxidation of the T_2 phase to yield TiO_2, SiO_2 and B_2O_3 is strongly favored over the formation of MoO_3.

For a coated LPBF Mo-3.3Si-4.5B-10Ti sample oxidized at 800 °C for 100 h, the microstructure is similar to the arc-melted sample after 800 °C for 50 h. Figure 7 shows coated LPBF Mo-3.3Si-4.5B-10Ti sample oxidized at 800 °C and 1300 °C for 100 h.

During thermal cycling, some samples exhibited early failure as indicated in Fig. 8a. The arrow indicates failure at the sample edge which progressed inward. While the flat portion of the sample exhibited self-healing during cycling, the failure at the sample edge is related to both the stress concentration due to the coefficient of thermal expansion mismatch within the layers which is enhanced at the edge and also due to the reduced coating thickness from pack cementation at the curved edge which limits the self-healing capability. Due to variations in sample preparation, some regions of high curvature result in thinner coatings which can be addressed with more optimized coating application. A portion of the flat region of the coated sample which remained intact throughout the entire 180 thermal cycles is shown in Fig. 8b. The coating remains thick, and the self-healing ability remains.

For the uncoated samples, the typical microstructure before complete failure is presented in Fig. 9a. In the cross-sectional image, it is apparent that the continuous outer scale is disrupted to provide channels for ingress of oxygen and volatilization of MoO_3. In order to analyze the linear mass loss of the uncoated sample, the Hertz–Knudsen–Langmuir vaporization equation was used as a model as shown in Eq. 1 and Fig. 9b [19]. J_v is the flux in terms of number of particles of MoO_3 being removed from the substrate. α_k is a modified vaporization coefficient, α_v, where $\alpha_k = k\alpha_v$. The mobility of MoO_3 is severely limited in two ways. The first is that the substrate only contains 82.2 at. % Mo and 17 area percent T_2 phase. The second consideration is that the surface is also partially covered by SiO_2 and TiO_2, shown in Fig. 8b. We find experimentally that $\alpha_k = 0.0025$, which is reasonable compared to known literature values [20]. P_E is the equilibrium vapor pressure of MoO_3 gas at 1300 °C. N_A is Avogadro's number. M is the molar mass of MoO_3. R is the gas constant, and T is temperature in Kelvin. From this calculation, the flux is 7.39×10^{21} particles/m²s or a mass loss of -0.145 mg/cm²s. A plot of this model is shown against both arc-melted and LPBF samples in Fig. 8a. This calculated mass loss fits the linear region of mass loss at the onset of oxidation well for both the arc-melted and LPBF uncoated samples and confirms that the main cause for failure of the uncoated samples is due to MoO_3 vaporization.

$$J_v = \frac{\alpha_k P_E N_A}{\sqrt{2\pi M R T}} \tag{1}$$

Conclusion

The oxidation behavior of a Mo-3.3Si-4.5B-10Ti alloy was examined during both isothermal exposure and thermal cycling across temperatures ranging from 800 to 1300 °C. Test samples were manufactured through arc melting and laser powder bed fusion (LPBF). Both types of samples exhibited a similar microstructure morphology with Mo dendrites and interdendritic T_2 phase and different size scales of 4 μm and 400 nm, respectively. The uncoated alloys demonstrated catastrophic mass loss within 10 h of exposure. To address environmental threats, a three-step coating strategy was employed, involving a Mo precoat, Si and B co-deposition, and a conditioning step for the formation of a multiphase layered self-healing borosilica coating. The coated LPBF samples exhibited minimal isothermal mass loss at 1300 °C after 100 h, with only minor mass gain observed under cyclic thermal loading after 345 cycles. During cyclic tests, the coating displayed a self-healing mechanism, with cracks filled with borosilica contributing to prolonged environmental resistance. Further work is necessary to evaluate the effects of water vapor exposure on the oxidation of Mo-Si-B-Ti alloys.

Author contribution JHP and DJT obtained funding, supervised the research plans, conducted data analysis and manuscript writing; LL, LW, TD and PN carried out experiments, data analysis and manuscript writing; and FZ and CZ performed thermodynamic calculations.

Data availability No datasets were generated or analyzed during the current study.

Declarations

Conflict of interest The authors declare no competing interests.

References

1. D. M. Dimiduk and J. H. Perepezko, *MRS Bulletin* **28**, 2003 (639).
2. J. H. Perepezko, *Science* **326**, 2009 (1068).
3. W. O. Soboyejo, and T. S. Srivatsan, eds. Advanced structural materials: properties, design optimization, and applications. CRC press, 2006.
4. P. Jain and K. S. Kumar, *Acta Materialia* **58**, 2010 (2124).
5. S. Burk, G. Bronislava, and C. Hans-Jürgen, *Acta Materialia* **58**, 2010 (6154).
6. L. Liu, C. Shi, C. Zhang, R. Su, H. Zhang, P. M. Voyles, and J. H. Perepezko, *Corrosion Science* **208**, 2022 110677.
7. D. Sturm, M. Heilmaier, Joachim H. Schneibel, P. Jéhanno, Birgit Skrotzki, and H. Saage, *Materials Science and Engineering: A* **463**, 2007 (107).
8. H. Nowotny, R. Kieffer, and F. Benesovsky, *Planseeber Pulvermetall* **5**, 1957 (86).
9. L. Liu, C. Sun, C. Zhang, P. M. Voyles, J. Fournelle, A. Handt, and J. H. Perepezko, *Scripta Materialia* **163**, 2019 (62).
10. L. Liu, C. Shi, C. Zhang, P. M. Voyles, J. H. Fournelle, and J. H. Perepezko, *Intermetallics* **116**, 2020 (106618).
11. R. Su, L. Liu, and John H. Perepezko, *International Journal of Refractory Metals and Hard Materials* **113**, 2023 (106199).

12. J. H. Perepezko and C. Harris, *Oxidation of Metals* **96**, 2021 (323).
13. I. P. Downs, J. H. Perepezko, R. Sakidja, and S. R. Choi, *Surface & Coating Technology* **239**, 2014 (138).
14. R. Su, H. Zhang, L. Liu, and J. H. Perepezko, *Corrosion Science* **221**, 2023 111365.
15. Z. Islam, M. Amalraj, L. Liu, L. D. Marks, J. H. Perepezko, and D. J. Thoma, *JOM* **75**, 2023 (5037).
16. R. Sakidja, J. H. Perepezko, S. Kim, and N. Sekido, *Acta Materialia* **56**, 2008 (5223).
17. Pandat Software: Software for thermodynamic calculations and kinetic simulations; CompuTherm LLC, www.computherm.com.
18. PanRHEA: Thermodynamic database for multicomponent refractory high-entropy alloys, CompuTherm LLC, www.computherm.com.
19. N. Hannay, *Treatise on Solid State Chemistry*: Vol. 4. Reactivity of Solids. Springer Science & Business Media, 2012.
20. B.V. L'vov, *Thermal Decomposition of Solids and Melts*, vol. 7. Springer, 2007.

Authors and Affiliations

Longfei Liu[1] · Liam F. Wood[1] · Phalgun Nelaturu[1] · Tianrui Duan[1] · Chuan Zhang[2] · Fan Zhang[2] · Dan J. Thoma[1] · John H. Perepezko[1]

✉ John H. Perepezko
perepezk@engr.wisc.edu

Longfei Liu
lliu329@wisc.edu

Liam F. Wood
lfwood2@wisc.edu

Phalgun Nelaturu
pnelaturu@wisc.edu

Tianrui Duan
tduan4@wisc.edu

Chuan Zhang
chuan.zhang@computherm.com

Fan Zhang
fan.zhang@computherm.com

Dan J. Thoma
dthoma@wisc.edu

[1] Department of Materials Science and Engineering, University of Wisconsin—Madison, 1500 Engineering Drive, 1212 Engineering Research Building, Madison, WI 53706, USA

[2] CompuTherm LLC, 8401 Greenway Blvd, Middleton, WI 53719, USA